





# Cellular structural and functional imaging of donor and pathological corneas with label-free dual-mode full-field optical coherence tomography

KEYI FEI,<sup>1,†</sup> ZHONGZHOU LUO,<sup>1,†</sup> YUPEI CHEN,<sup>1</sup> YUANCONG HUANG,<sup>1</sup> SAIQUN LI,<sup>1</sup> VIACHESLAV MAZLIN,<sup>2</sup>  ALBERT CLAUDE BOCCARA,<sup>2</sup> JIN YUAN,<sup>1,3</sup> AND PENG XIAO<sup>1,4</sup> 

<sup>1</sup>State Key Laboratory of Ophthalmology, Zhongshan Ophthalmic Center, Sun Yat-sen University, Guangdong Provincial Key Laboratory of Ophthalmology and Visual Science, Guangzhou 510060, China

<sup>2</sup>Institut Langevin, ESPCI Paris, PSL Research University, CNRS, 1 rue Jussieu, Paris 75005, France

<sup>3</sup>yuanjincornea@126.com

<sup>4</sup>xiaopengaddis@hotmail.com

<sup>†</sup>These authors contributed equally to this work.

**Abstract:** In this study, a dual-mode full-field optical coherence tomography (FFOCT) was customized for label-free static and dynamic imaging of corneal tissues, including donor grafts and pathological specimens. Static images effectively depict relatively stable structures such as stroma, scar, and nerve fibers, while dynamic images highlight cells with active intracellular metabolism, specifically for corneal epithelial cells. The dual-mode images complementarily demonstrate the 3D microstructural features of the cornea and limbus. Dual-modal imaging reveals morphological and functional changes in corneal epithelial cells without labeling, indicating cellular apoptosis, swelling, deformation, dynamic signal alterations, and distinctive features of inflammatory cells in keratoconus and corneal leukoplakia. These findings propose dual-mode FFOCT as a promising technique for cellular-level cornea and limbus imaging.

© 2024 Optica Publishing Group under the terms of the [Optica Open Access Publishing Agreement](#)

## 1. Introduction

The cornea is a transparent avascular connective tissue located in the front of the eye [1]. It acts as the primary barrier to protect the eye from foreign bodies and provides 2/3 of the total refractive power of the eye [2]. It is composed of five main layers: the epithelium, Bowman's layer, stroma, Descemet's membrane, and endothelium [3]. Each layer plays an important role in maintaining normal physiological function of the cornea. Any pathological alterations in the cornea, such as cell dysfunction, collagen fiber structure arrangement disorder, etc., may result in severe clinical problems including the loss of corneal transparency, resulting in visual impairment or blindness. The cornea's outermost layer, the epithelium, which has 5-7 layers of cells, with a thickness of 50-60  $\mu\text{m}$ , consisting of surface squamous cells, intermediate wing cells, and inner basal cells [3], has attracted much attention in basic research on corneal diseases due to its ability to regenerate and repair. The corneal epithelium acts as a barrier against liquid and microbial penetration, thereby maintaining corneal transparency and protecting the eyes from external environmental influences [4]. The corneal epithelium maintains a homeostatic state through a comprehensive process of cell proliferation, migration, differentiation, stratification, and apoptosis, with the surface epithelial cells continuously desquamating [5-7]. After experiencing trauma, microbial infection, or surgical injury, the corneal epithelium initiates a sequence of wound healing procedures that aim to re-establish barrier function and thwart potential opportunistic infections that may result in eye damage and vision loss. Another crucial structure for corneal regeneration and repair is the limbus, located in the transition zone between the transparent cornea and the

white sclera, which contains a group of self-renewing stem cells located in the basal epithelial layer of the limbus within the cell niche, called limbal epithelial stem cells/progenitor cells (LSCs) [8–10]. Evaluating the structural and functional changes of the cornea and limbus, and detecting pathological changes in tissues, especially the functional detection of epithelial cells, is of great significance for exploring the pathogenesis of ocular surface diseases and monitoring the progression of diseases.

In recent years, novel non-invasive high-resolution imaging methods in ophthalmology have offered direct and objective proof of the structural and functional imaging of the cornea and limbus. Clinical anterior segment optical coherence tomography (AS-OCT) [11,12] can provide cross-sectional tomographic imaging of the cornea to determine the depth of disease involvement, but an unmet need for cellular resolution to analyze the pathological changes of cornea and limbus tissues. In vivo confocal microscopy (IVCM) [13] can obtain micrometer-level resolution imaging features of cells and nerves on the ocular surface but works in a contact manner and provides a small field of view (FOV) (below  $0.4\text{ mm} \times 0.4\text{ mm}$ ) without the ability of three-dimensional (3D) imaging, which limit its application to some extent in clinics. In recent years, high-resolution OCT technology has significantly improved the quality and efficiency of ophthalmic imaging, especially in the context of the cornea. The development of point scanning spectral-domain OCT (SD-OCT) [14–17] using broadband light sources have achieved ultrahigh resolution in the order of  $1\mu\text{m}$ , acquiring volumetric SD-OCT images of human cornea with cellular structures, nevertheless suffer noticeable motion artefacts due to relative low scanning rate. Line-field SD-OCT (LF-SD-OCT) [18–20] using cylindrical lens or Powell lens accelerates data acquisition by capturing images along lines rather than point-by-point, in combination with high spatial resolution, LF-SD-OCT allows volumetric visualization of corneal cellular structures. Full-field optical coherence tomography (FFOCT) is an *en face* variant of OCT [21]. Time-domain FFOCT uses full-field illumination of a spatial incoherent light source to obtain a large-field *en face* image with micron-scale 3D resolution and its image resolution is relatively insensitive to optical aberrations [22–24]. In recent years, FFOCT has been successfully applied in ophthalmic imaging to achieve high-resolution imaging of cellular structure, nerve fiber morphology, and vascular distribution of the eye, especially in cornea and limbus [25–28]. There are also Full-field swept-source OCT (FF-SS-OCT) systems, which use tunable light source, offering high-resolution volumetric images of human cornea [29]. Nevertheless, FF-SS-OCT has limited axial resolution ( $\sim 5\mu\text{m}$ ), making it difficult to resolve the precise structure of thin cornea layers such as endothelium.

Due to the advancement of optical imaging technology, imaging research is experiencing rapid development from “structural imaging” to “functional imaging”. Increasing demands are also being placed on corneal imaging methods and techniques for basic research and early diagnosis of corneal diseases. The development of high-resolution imaging techniques for the cornea and limbal tissues is an imperative research area within the interdisciplinary field of ophthalmology and imaging. These methodologies offer enhanced precision and efficacy in imaging, facilitating the diagnosis and analysis of corneal pathogenesis, along with comprehensive assessments of ultrastructural and functional alterations.

While conventional OCT only provides static structural information based on sample refractive index gradient, dynamic OCTs have been invented to visualize the intratissue and intracellular activities by analyzing the time sequence of OCT images. Dynamic SD/SS-OCT have been applied for ex vivo and in vitro sample such as tumor spheroids, human esophageal, as well as mouse airway and cornea [30–32]. For FFOCT, a novel method namely dynamic FFOCT (D-FFOCT) [33] has also been developed to obtain the sub-cellular contrast based on spatio-temporal signals complementary to FFOCT static images by collecting and analyzing the temporal fluctuations of backscattered light from tissue and cells. D-FFOCT visualizes the functional information of subcellular metabolic activities. Previous studies [34–37] have demonstrated

the utility of D-FFOCT in distinguishing between diverse cellular states (such as normal, dead, or dying cells), and the signal performance of different cell types in D-FFOCT images varies, which is closely related to the activity of intracellular organelles. The application of D-FFOCT to retinal organoids and diverse cells has demonstrated its great potential for cell classification and cell status evaluation. Nevertheless, investigation of D-FFOCT in normal and pathological corneal tissues and limbus has not been demonstrated yet.

In this investigation, a dual-mode Full-Field Optical Coherence Tomography (FFOCT) system was devised for the performance of both static and dynamic cellular imaging, and imaging experiments were meticulously executed on donor corneal grafts, limbus and *in vitro* pathological corneal samples including keratoconus and corneal leukoplakia tissues. The study aimed to elucidate structural and functional variances evident in cornea and limbus through dual-mode FFOCT images at the cellular level, with a particular emphasis on unveiling nuanced insights within dynamic signals. The findings of our research reveal that while static FFOCT images effectively depict relatively inert structures such as corneal stroma, scar fibers, and nerve fibers, D-FFOCT emerges as instrumental in accentuating intracellular contrast resulting from metabolic activity changes. This supplementation contributes specific valuable functional information regarding corneal epithelial cells. Notably, the dual-mode FFOCT images showcased distinctive structural and dynamic disparities in pathological changes between normal and diseased corneas at the cellular level, without the necessity of contrast agent labeling.

## 2. Material and methods

This present study was performed at the Zhongshan Ophthalmic Center (Sun Yat-Sen University in Guangzhou, China) in accordance with the declaration of Helsinki. It was approved by the Institutional Review Board of Zhongshan Ophthalmic Center (2022KYPJ138). Subjects were informed of the aim of the study and all consents were obtained.

### 2.1. Dual-mode FFOCT setup

Based on optical plane interference for imaging live cells within *in vitro* tissues, the hardware of dual-mode FFOCT system is designed using the same principles as traditional time-domain FFOCT system [21,33]. As shown in Fig. 1(A), in the Linnik interferometric system, a light emitting diode (LED) with a central wavelength of 660 nm (M660L3, Thorlabs) serves as a spatially incoherent broadband light source. The LED light travels through an aspherical condensing lens and is then evenly split (50/50) via a cubic beamsplitter into the sample and reference arms with identical high-NA microscope objectives (NIR APO 40x, 0.8 NA, Nikon) and focused to the sample tissue and reference mirror. The sample stage is supported by a high-precision motor for micro-scale depth scanning to achieve 3D imaging. The reference mirror is mounted on a piezoelectric transducer (PZT) for optical path-length (OPL) modulation in static FFOCT imaging mode. The light signals scattered backward from the sample arm at different depths and the light signals reflected by the mirror in the reference arm are recombined by the beamsplitter, passing through the camera tube lens, and finally detected by a complementary metal-oxide-semiconductor (CMOS) camera (Q-2A750-Hm/CXP-6, Adimec) with  $1440 \times 1440$  pixels and large full well capacity. Images are recorded when the OPL of the reference arm and the sample arm are identical with the focal plane matched with the coherence plane. The whole system is placed on a suspended anti-vibratory platform to ensure steady image acquisition, thereby minimizing environmental interference signals. With the high-magnification high-NA objectives used in our dual-mode FFOCT system, a lateral resolution of  $0.5 \mu\text{m}$  is ensured, which is sufficient to distinguish the cellular structures of the cornea and limbus. The system achieves an axial resolution of  $1.7 \mu\text{m}$  owing to the depth of focus of the microscope objectives ( $1.7 \mu\text{m}$ ) is smaller than the coherence length of the LED light source ( $7.7 \mu\text{m}$ ). Together with the camera tube lens, the system provides a field of view of  $320 \mu\text{m} \times 320 \mu\text{m}$ .

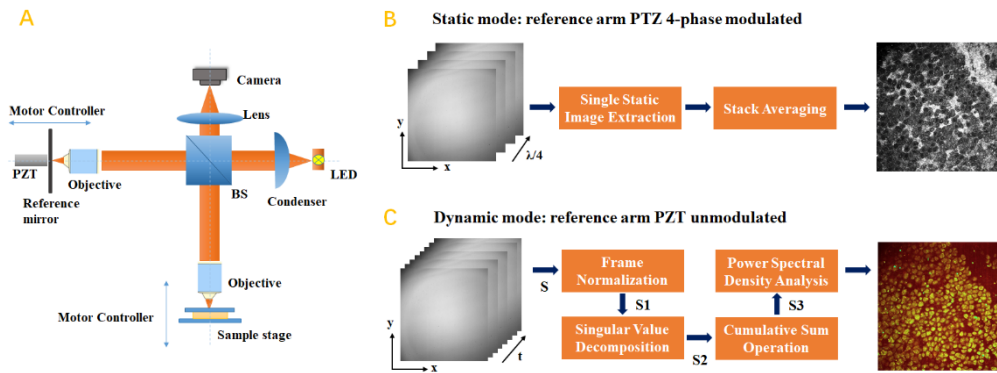


**Fig. 1.** Schematic of the dual-mode FFOCT system and imaging processing workflow. A: schematic of the dual-mode FFOCT setup based on Linnik interferometer. B: in static mode, four-phase modulation scheme is applied with reference arm PZT to extract single static image, and multiple static FFOCT images are acquired and averaged to improve SNR. C: in dynamic mode, a time-series of interferograms are acquired without reference arm modulation, then undergo frame normalization, singular value decomposition for motion artifacts removal, cumulative sum operation for SNR improvement and finally power spectral density analysis to obtain the dynamic FFOCT images. BS: Beam splitter; PZT: Piezoelectric transducer; LED: light emitting diode.

## 2.2. Human corneas sample preparation

This study was based on a collection of 10 human corneoscleral rings from donors in the eye bank (Guangdong Eye Bank, China), 5 keratoconus samples and 5 corneal leukoplakia samples from patients, which were discarded after corneal transplantation. All procedures were based on standard operating protocols specified by the Chinese Eye Bank Association. The donor corneoscleral rings after transplantation still retain the marginal 2-5 mm corneal tissue and the complete limbus, which were still representative tissues for the study of the cornea and limbus structure. Pathological corneal samples were obtained through routine cutting during surgery without causing additional damage to the sample. All samples were stored in Optisol-GS immediately after the intraoperative cutting was completed and preserved at low temperature for transportation, and dual-mode FFOCT imaging was performed on the specimens within 4 hours after cutting. During the image acquisition process, the tissue was sandwiched securely in a transparent vessel containing Optisol-GS to ensure tissue activity. The image acquisition time was less than 2 hours, and once completed, the specimens were immediately handed over to the laboratory sample recycling area for further processing.

## 2.3. Dual-mode FFOCT image acquisition and data processing

For each area of interest, 3D stack of both static and dynamic FFOCT images were captured with  $1\ \mu\text{m}$  step size throughout the whole depth of the sample. A translational stage was also employed to adjust the imaging area with symmetrical positions chosen randomly in each sample. When collecting signals at different imaging depths, the separation of the focal and coherence planes may occur due to the difference in the refractive indices between the imaging medium and the sample. Thus, we have applied a former developed defocus correction algorithm [38] to compensate the mismatching at each imaging depth with corneal refractive index ( $\sim 1.376$ ) and water refractive index ( $\sim 1.333$ ) incorporated.

For static FFOCT image acquisition, as illustrated in Fig. 1(B), traditional four-phase modulation scheme was applied with the reference mirror shifted consecutively by the PZT with a phase shift of  $\pi/2$  [22]. The camera was set at a frequency of 100 Hz and synchronized with the modulation

of the reference mirror, result in a frame rate of 25 Hz for single static image acquisition. To improve the image signal to noise ratio (SNR), in this study, 50 static images of each imaging plane were consecutively captured and averaged. The averaged static FFOCT images were presented with a logarithmic lookup table in a 256-grayscale image, where a high reflectance was displayed as white against the black background.

For dynamic FFOCT image acquisition, as shown in Fig. 1(C), the reference mirror was set to unmodulated, recording only a time series of the interferograms over a short period, thereby exhibiting solely the interfering signal variations of the internal motions of the sample. In this study, 512 interferograms were acquired, also at a frequency of 100 Hz, right after the static FFOCT image acquisition in each imaging plane, obtaining a (1440,1440,512) raw interference signal set (S). Former publications of our collaborators have described the following processing algorithm of dynamic FFOCT images in detail [36]. Normalization of each acquired frames was firstly conducted in order to compensate the camera's frame-to-frame instability induced by exposure time variations, which were typically resulted from the unstable sensor performance as well as its reaction error to the high frequency camera triggering signal, etc. Since the targeted dynamic signal is typically weak, it can be easily buried by external motions and suffers lower SNR when imaging deep. To resolve these obstacles, a motion artifact removal and signal enhancement algorithm was then adapted and applied sequentially to the normalized interference signal set (S1). The principle and mathematic derivation process of this motion artifact removal and signal enhancement algorithm can be referred to the publication of Scholler [39]. In brief, a singular value decomposition (SVD) based adaptive threshold filtering method was used to remove artifact arising from sample or mechanical motion during data acquisition, resulting in the filtered interference signal set (S2), and a cumulative sum operation by applying window processing in the time dimension and calculating the average of the cumulative sum of signals within the window was performed to enhance the SNR of weaker dynamic signals, resulting in the enhanced interference signal set (S3). Subsequently, the power spectrum density (PSD) for each pixel in the enhanced interference signal set (S3) was computed using Welch's method to extract the frequency characteristics of the dynamic signal and further encoded through the Hue-Saturation-Value (HSV) color space, which was an orthogonal color space that provides three different channels to calculate different physical parameters, thus obtaining a three-dimensional color image. The average frequency of the signal was recorded in the hue channel, where the band corresponding to the low frequency (0–0.6 Hz) was encoded in the red channel, the band corresponding to the intermediate frequency (0.6–5.4 Hz) was encoded in the green channel, and the band corresponding to the high frequency (5.4–25 Hz) was encoded in the blue channel. The saturation channel was encoded through the reciprocal value of each voxel's frequency bandwidth. This means that a narrow bandwidth with high saturation creates vivid colors while vice versa creates a greyish appearance. The value channel was composed of the standard deviation of the moving window of 50 images to highlight the ultimate intensity of intracellular motion. Finally, the three channels were merged to form a color image that depicts the dynamic profile of the imaged sample. For 3D stacks, we employ a rigid alignment strategy that relies on scale-invariant feature transform (SIFT) features and random sampling consensus algorithm to compensate any lateral drift present in the samples. The interference signal sets were processed by MATLAB (MathWorks) and our customized software, and each dynamic image process could be completed within 10 seconds. While this processing speed was not practical for real-time preview of dynamic image over a long period, interferometric signals acquired over a long period were divided into multiple short-term signals (typically 100 interferograms), which was used for continuous preview of dynamic images computed on the GPU.

#### 2.4. Dual-mode FFOCT image post-processing and quantitative analysis

With the static and dynamic FFOCT images extracted, FIJI [40] was further employed for better image visualization and quantitative analysis. Functional imaging, due to its sensitivity to subtle fluctuating signals, was susceptible not only to perturbations from environmental factors during acquisition, but also sensitive to the movements of the impurities and scattering particles inside the immersion media, potentially leading to spurious signals that deviate significantly from the intrinsic dynamics of the samples. To enhance the realistic interpretation of the images, besides of the SVD algorithm applied during the image processing, we remove artifact signals that may interfere with image interpretation semi-automatically. Adjustments of image brightness and contrast can also be used as needed, and Gaussian blur method could be applied to further denoise the images. For three-dimensional image stacks, the Z-stack browsing feature can facilitate observation. The StackReg plugin was employed for automatic registration of 3D stacks with lateral position jittering, although this step may not be necessary for all images. These strategic application of image processing tools was instrumental in eliminating extraneous noise, thereby safeguarding the integrity of the pertinent information contained within the images. The cells, nerve fibers, and other structures are distinguished from the background using automatic or manual thresholding methods. Various parameters such as area, diameter, cell count, and neuronal density are then calculated. Neuronal density refers to the length of neuronal fibers per unit area, expressed in micrometers per square millimeter. The Neuron J plugin is employed for automated tracking of neuronal fiber bundles, followed by manual calibration to measure the total length of neurons within the image.

### 3. Results

#### 3.1. Dual-mode FFOCT imaging of donor cornea

The dual-mode FFOCT device was used to simultaneously and sequentially collect high-resolution structure and function images of corneal tissue layers in all donor samples, ensuring that the *en face* static images of each layer are in the same position as the dynamic images and can be superimposed. All layers of the corneal sample (including the epithelium, Bowman's layer, and stroma) can be identified in the structural imaging. In our experiment, only the corneoscleral rings were obtained after donor corneal samples were utilized for penetrating or lamellar keratoplasty surgeries. The whole endothelial layers of the healthy donor cornea were typically extracted for other endothelial transplantation surgeries, or left damaged endothelium under the corneoscleral ring, rendering image capture unfeasible. Figure 2 shows the *en face* sections obtained by dual-mode FFOCT at a depth interval of 1  $\mu\text{m}$ , and the axial section of the donor cornea is reconstructed with the 3D stack. In the static image obtained through FFOCT, discrete cellular entities within the squamous cell, wing cell, and basal epithelial cell layers are discernible. The superficial squamous cells (see Fig. 2(A)) exhibit distinct high reflective cell boundaries, with variable cell sizes and some cells presenting high reflective nuclei. The shape of wing cells (see Fig. 2(D)) is polygonal, with high reflection of cell boundary, low reflection of cell body, invisible nucleus, and tightly arranged between cells. The densely arranged basal cells (see Fig. 2(G)) are irregular in shape with the smallest size among epithelial cells, which show bright and dusky alternating cell reflection. In the D-FFOCT image, corneal epithelial cell images can be displayed. In each layer of epithelial cells (see Fig. 2(B), (E), (H)), local fluctuations of time-varying interference signals within the cells are collected and processed to show high signals in the dynamic images which are co-located with corneal epithelial cells in static images, while low signals are displayed without interference changes outside the cells. We found that dynamic images highlight the distribution, size, and shape of epithelial cells to a greater extent than static images. The static images were defined as the red channel and the co-located dynamic images were defined as the green channel, before being superimposed. The resulting superimposed

images (see Fig. 2(C), (F), (I)) better illustrate the disparities between the structural and dynamic images, particularly with regard to epithelial cells. Based on the experimental results, we found that certain cells can be displayed in the static images but not in the dynamic images (indicated by the black circle in Fig. 2(C)). Additionally, there may be differences in cell size and shape between the two images (indicated by the white circle in Fig. 2(C)). D-FFOCT imaging identifies the intracellular time-varying fluctuations of interference signals as active signals. It was discovered that functional signals may be different between various layers of epithelium within the same sample. The functional signal frequency within the superficial epithelium (see Fig. 2(B)) is notably lower than that of intermediate wing cells (see Fig. 2(E)) and basal cells (see Fig. 2(H)). This suggests that interference signals fluctuate faster in the deeper epithelium than in the superficial layer. In the structural *en face* image, the corneal subbasal nerve plexus (SNP) (see Fig. 2(J), (P)) presents a highly reflective structure, with Y-shaped bifurcation and H-shaped nerve fiber bundles connected, and the nerve fiber structure is visible to enable objective density measurement. However, in the functional imaging (see Fig. 2(K)), nerve fibers cannot be visualized, while the weak backscattered basal cells masked by high reflexes are highlighted. The Bowman layer of the normal donor cornea is intact and has a homogeneous moderate reflection in the *en face* structure view (see Fig. 2(Q)), with keratocytes and nerve fibers faintly visible. Stromal keratocytes and lamellae of collagen bundles form a dense network, linked by cytoplasmic cell protrusions between adjacent keratocytes, and occasionally traversed by nerve fibers, as shown in Fig. 2(R). Figure 2(M) illustrates activated stromal cells appearing as high reflectivity in static image, characterized by elongated, often intertwining cell contours, exhibiting polygonal or crab-like shapes. Owing to enhanced cellular reflectance, the nuclei of stromal cells are scarcely discernible. Circular hyper-reflective immune cells are also observable within the stroma. In the corresponding dynamic image (see Fig. 2(N)), static stromal cell structures are nearly obliterated, revealing only active immune cells. Discrimination between cell bodies and nuclei is feasible based on functional signal manifestation. Figure 2(S) shows a tomographic image of the donor cornea projected on a perpendicular plane. The characteristic stacked organization is characterized by regular corneal epithelium, homogeneous high-reflection in the Bowman layer, and bright, slender profile arrangement of keratocytes parallel to the corneal surface. Figure 2(T) shows a three-dimensional stack of *en face* static images of the donor cornea. Figure 2(U) shows a three-dimensional stack of *en face* dynamic images of donor corneal epithelium.

### 3.2. Performance of keratoconus in dual-mode FFOCT imaging

The thickness of the keratoconus epithelium is irregular. FFOCT scans the keratoconus samples thoroughly from top to bottom with micrometer resolution, and the reconstructed cross-sectional structural map (see Fig. 3(A), (D), (F)) can clearly distinguish the rupture and loss of the Bowman layer, as well as the cracks between the epithelial and stromal layers. At the same time, FFOCT can also achieve accurate measurements of the thickness of various parts of the cornea. By processing and calculating the image of the basal nerve of the keratoconus (see Fig. 3(B)), it can be observed that the basal nerve of the keratoconus is coarsely curved with a calculated nerve density of  $22480.5 \mu\text{m}/\text{mm}^2$ . The volume of keratocytes in keratoconus is significantly atrophied, the cell processes are slender, and occasionally the stromal nerves are thick and branched (see Fig. 3(C)). In the longitudinal section, it can be observed that the lacunae between stromal cells increase, the gaps between lamellae increase, and the matrix arrangement is irregular (see Fig. 3(A)). Therefore, FFOCT has significant advantages in determining changes in corneal stromal fibers, whether in terms of changes in the connection between horizontal keratocytes or the arrangement of longitudinal lamellae. In severe keratoconus, there may be rupture of the Bowman layer (see Fig. 3(A)), preservation of the Bowman layer (see Fig. 3(D)), loss of the Bowman layer (see Fig. 3(F)), and the presence of keratocytes in the epithelium (see Fig. 3(E)). However, there is

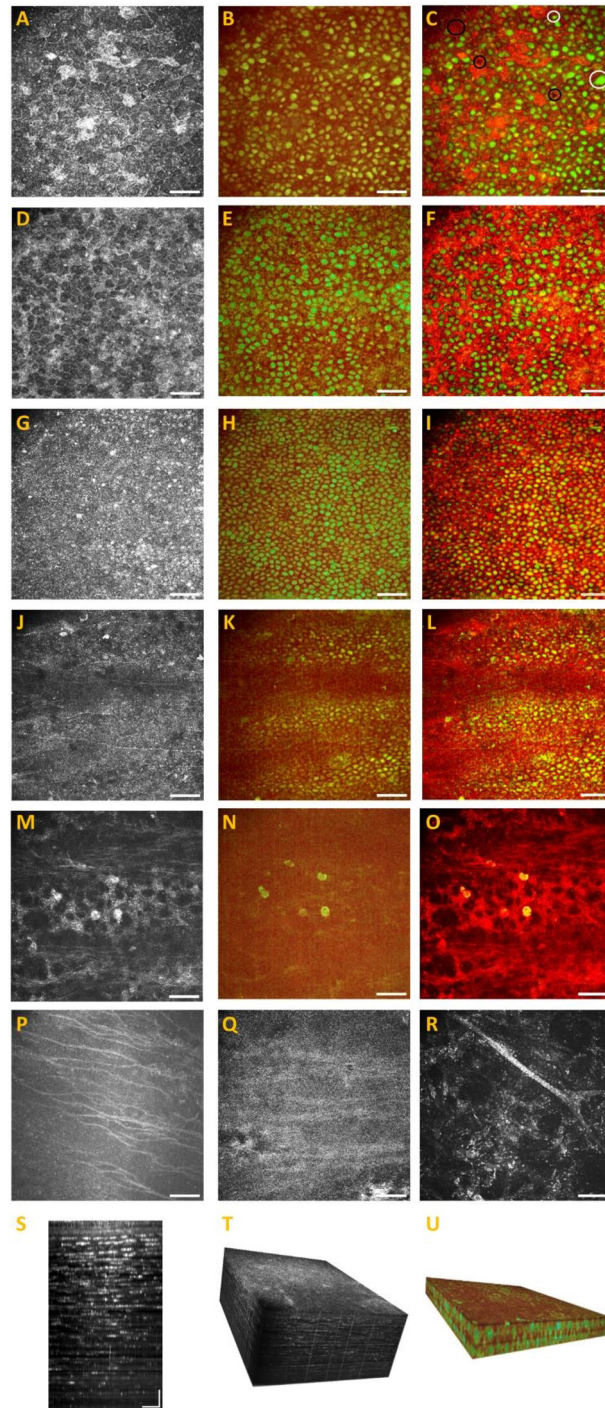


**Fig. 2.** Dual-mode FFOCT imaging of donor cornea. A, B, C: squamous epithelial cell layer. D, E, F: wing epithelial cell layer. G, H, I: basal epithelial cell layer. J, K, L: subbasal nerve layer. M, N, O: stromal layer. P: static image of subbasal nerve plexus (SNP). Q: static image of Bowman's layer. R: corneal nerve traversing through the stroma. S: tomographic image of a donor cornea approximately 550  $\mu\text{m}$  thick. T: 3D stack of *en face* static images of a cornea approximately 550  $\mu\text{m}$  thick. U: 3D stack of *en face* dynamic images of corneal epithelium approximately 40  $\mu\text{m}$  thick. (Scale-bar: 50  $\mu\text{m}$ )



a gap between the epithelium and the stroma, which cannot be filled by keratocytes that break into the corneal epithelium. Therefore, the presence of this gap may be a better indicator of the severity of keratoconus than the changes in the Bowman layer.

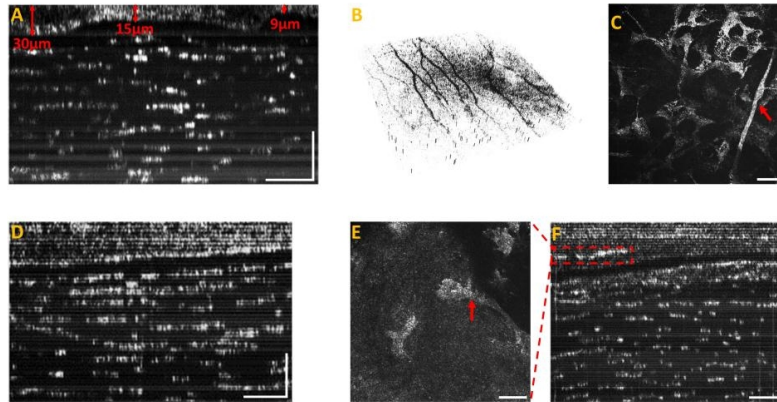


**Fig. 3.** FFOCT static images of keratoconus samples. A: tomographic image with irregular epithelial thickness (9-30  $\mu\text{m}$ ). B: basal nerve distribution. C: stroma layer, arrow refers to stromal nerve. D: a gap between the epithelium and stroma. E: en face image of stromal cells breaking into the epithelial layer. The arrow points to the keratocyte. F: bowman's layer loss. (Scale-bar: 50  $\mu\text{m}$ )

The apoptosis of corneal epithelial cells is a sign of epithelial changes in keratoconus, especially at the apex of the cone. Condensed circular and small deep reflection structures are visible in the shallow epithelial cells when examining the static image of keratoconus epithelium (see Fig. 4(A), (C)). Meanwhile, the dynamic image highlights that this structure is located within the functional signal of epithelial cells (see Fig. 4(B), (D)), showing low signal or loss. The distribution of basal epithelial cells is uneven due to the irregular changes in the Bowman's layer. In the static images (see Fig. 4(E)), except for the decrease in density, the reflectivity, size, and shape of basal epithelial cells do not show significant changes. In the dynamic images, some basal epithelial cells have lost their functional signals (see Fig. 4(H)) which only display the outline of the cell structure (see Fig. 4(G)). Epithelial cells with varying characteristics are present in a keratoconus sample. As shown in the black box of Fig. 4(I) (local magnification as Fig. 4(K)), the epithelial cells appear homogeneous reflection with indistinct cell boundaries, while in the corresponding dynamic image (see Fig. 4(M)) appears homogeneous and intact intracellular signals. The individual cells' functional signals can be detected entirely. As shown in the red box of Fig. 4(I) (local magnification as Fig. 4(L)), the boundaries of epithelial cells are clear, and there are highly reflective nuclei within the cells. Additionally, both the cell and the nucleus appear swollen. In the corresponding dynamic image (see Fig. 4(N)), the cytoplasmic functional signals are lost, while the nuclei can show moderate signals, signal reduction, or loss.

Table 1 presents the preliminary quantitative analysis results of the morphological parameters of the imaged keratoconus tissues in comparison to the donor corneas. Due to the absence of the endothelial layer in samples and the incomplete stroma layer post lamellar transplantation surgery, we show only parameters of the corneal epithelial layer and Bowman's layer, including cell density, cell diameter, epithelial thickness, Bowman's layer thickness, and nerve density. Note that the cell density was calculated based on dynamic images, while thickness, diameter, and nerve density were calculated based on static images. Given the limited sample size, it is not feasible to control influencing variables such as age, gender, imaging location, etc., thus we are currently unable to perform comparative statistical analysis between donor corneas and

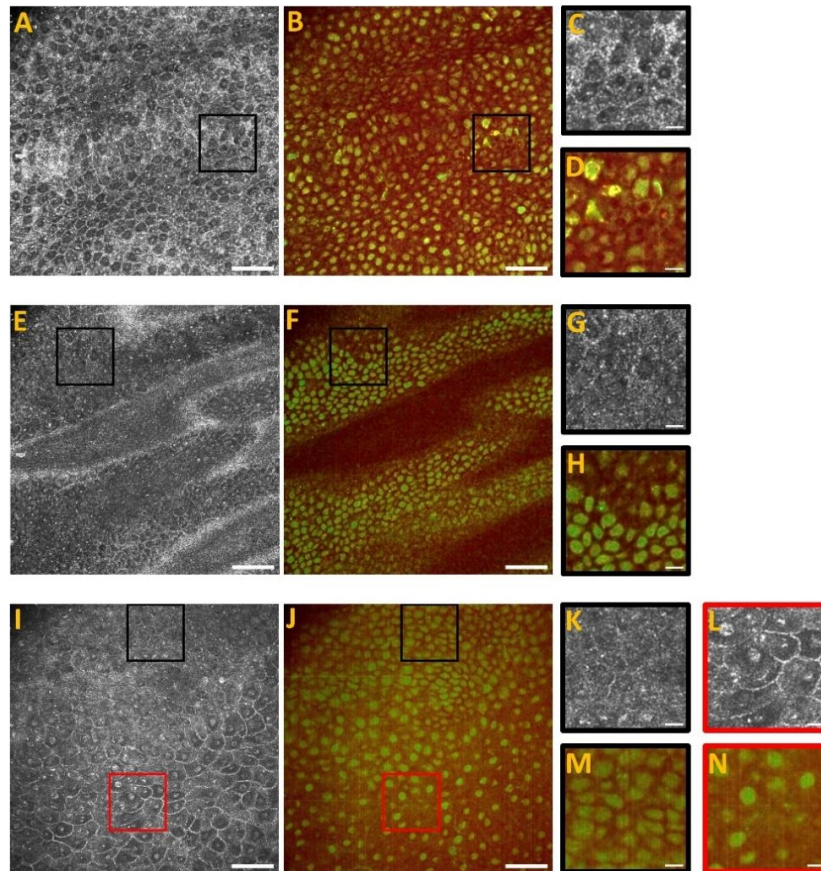


**Fig. 4.** Dual-mode FFOCT imaging of keratoconus epithelial cells. A, B: superficial epithelial cells. C, D: zoomed images of the ROIs marked in A and B. E, F: basal epithelial cells. G, H: zoomed images of the ROIs marked in A and B. I, J: manifestations of keratoconus epithelial cells. K-N: zoomed images of the ROIs marked in I and J. (Scale-bar: A, B, E, F, I, J 50  $\mu\text{m}$ ; C, D, G, H, K, L, M, N 10  $\mu\text{m}$ )

keratoconus samples. Nevertheless, the acquired parameters are all in accordance to those reported in literatures [41–43].

### 3.3. Performance of inflammatory lesions in corneal leukoplakia on dual-mode FFOCT imaging

In corneal leukoplakia samples, due to the change of corneal refractive index caused by corneal scar formation, the diagnosis of corneal leukoplakia is clear based on the FFOCT longitudinal section image formed by light reflection (see Fig. 5(A)), and corneal neovascularization or lymphatic vessels can be seen at the scar (see Fig. 5(B)). Due to the occurrence of inflammation, the corneal epithelium exhibits inconsistent changes in different cases and between different layers. When the corneal epithelial inflammation is severe, the basal cells exhibit a highly edematous and highly reflective structure (see Fig. 5(C)), and a large number of Langerhans cells can be seen below the basal layer (see Fig. 5(D)). The opacity of scar tissue impacts the extraction of deep information and weak interference signals, along with the loss of epithelial cells in severely diseased tissues. Consequently, the quality of imaging for severely scarred corneal tissues with dual-mode FFOCT is poor, especially for dynamic images. In instances

**Table 1. Quantification of Morphometric Parameters in Donor Cornea and Keratoconus**

Morphological Parameters	Donor cornea (corneoscleral ring)	Keratoconus
The density of squamous cell (/mm <sup>2</sup> )	2172.6 ± 1401.2	2350.7 ± 636.7
The density of wing cell (/mm <sup>2</sup> )	5532.8 ± 871.9	5169.9 ± 1120.4
The density of basal cell (/mm <sup>2</sup> )	9085.2 ± 932.7	8190.7 ± 1303.5
The diameter of squamous cells (μm)	8.1-30.7	7.3-32.4
The diameter of wing cells (μm)	8.9-15.3	7.5-16.2
The diameter and size of squamous cells (μm)	6.9 -13.1	7.1 -13.5
Basal nerve density (μm/mm <sup>2</sup> )	21007.25 ± 5703.23	15978.83 ± 9946.29
The epithelial thickness of the central cornea (μm)	-	11.5 ± 3.98
The epithelial thickness of the peripheral cornea (μm)	42.7 ± 5.36	38.5 ± 17.03
Bowman layer thickness (μm)	8-12	0-6

where tissue samples preserve the corneal epithelium, the imaging characteristics of epithelial cells manifest discernible variations both intralayer and interlayer, attributable to underlying pathological alterations. As shown in Fig. 6(A), in the superficial corneal epithelium, the scarred tissue exhibits a highly reflective acellular structure in the static image, corresponding to no functional signal in the dynamic image (see Fig. 6(B)), while epithelial cells can still display functional signals, with clear signals in the nucleus and indistinct cell boundaries. For basal epithelial imaging, the presence of non-transparent impurities in the corneal tissue weakened the clarity and contrast of the cell static images (see Fig. 6(C)). In the dynamic images (see Fig. 6(D)), basal epithelial cells with functional signals can be highlighted, whereas some cells in the basal layer appear deformed, elongated and irregular in shape, displaying stronger functional signals than those of the surrounding small and circular basal epithelial cells. In areas with mild inflammation, corneal epithelial cells may display various manifestations during the development of inflammation. As shown in Fig. 6(E), the swollen nucleus of corneal epithelial cells appears, the cell density decreases, and holes left after cell death appear. The dynamic images permit an examination of the intracellular changes (see Fig. 6(F)). As illustrated in Fig. 6(J), two cell clusters displaying active signals are visible in the magnified cell, suggesting that the cell is undergoing division. Figure 6(K) shows a poorly defined cell in the hole, with low and weak signals present in the cytoplasm, indicating that the cell may be in the late stage of apoptotic disintegration. The dynamic FFOCT image of the shrunken cell shown in Fig. 6(L) turns to be reddish with reduced brightness, indicating the interference signals shift to lower frequencies with damped variation amplitudes, which suggests that the cell may have reached a state of death. However, static images of these cells (Fig. 6(G), (H), (I)) cannot reveal any intracellular changes, and the variations between cell images are not characteristic. The changes in corneal epithelial cells caused by different degrees of lesions can be detected. Figure 6(M) shows the cell swelling (see magnified Fig. 6(O)), cell deformation in the scar transition zone (see magnified Fig. 6(P)), and wing cells with low reflection cell boundaries (see magnified Fig. 6(Q)). These observations are further supported by functional imaging of the corresponding corneal epithelium (see Fig. 6(N)). The functional signal of swollen cells is weakened and the cell contour is unclear (see magnified Fig. 6(R)), the deformed cells in the transition zone exhibit moderate functional signal (see magnified Fig. 6(S)), and wing cell functional signal with clear cell contour (see magnified Fig. 6(T)). In FFOCT structural images, corneal stromal scars are characterized by highly reflective, disorganized fibrous tissue (see Fig. 6(U)). In dynamic functional imaging, inflammation cells obscured by fibers become prominent (see Fig. 6(V)), as these cells exhibit certain functional activity and high reflective fiber functional states are more stable. Figure 6(W) and Fig. 6(X) show enlarged functional images of inflammatory cells, where the cytoplasm

displays highly dynamic and active functional signals, with the functional signals in the nucleus being weaker. Based on the shape, diameter, and morphology of the cells and nucleus, it is possible to approximately differentiate types of inflammation cells. Thus, dual-mode FFOCT imaging has significant potential in identifying the inflammatory processes in pathological tissues.

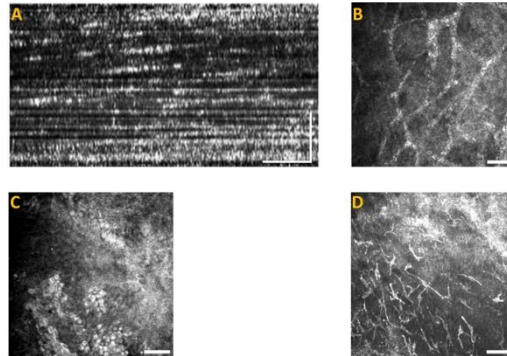


**Fig. 5.** FFOCT static images of corneal leukoplakia samples. A: tomographic image. B: corneal neovascularization or lymphatic vessels. C: edematous corneal basal cells. D: Langerhans cells below the basal layer. (Scale-bar: 50  $\mu\text{m}$ )

### 3.4. Dual-mode FFOCT imaging of the limbus

The characteristic structures of the limbus, limbal crypt, and limbus palisades, are distinguishable on dual-mode FFOCT images. In Fig. 7(A), the limbal crypt structure shows cells with multiple manifestations of highly reflective small cells represent melanosomes (shown in the black box, magnified in Fig. 7(B)), low-reflective irregularly shaped cells (shown in the red box, magnified in Fig. 7(C)), and cells with unclear cell boundaries and visible nuclei (shown in the yellow box, magnified in Fig. 7(D)). The limbal crypt is the niche structure of limbal stem cells, so a variety of cells in the crypt may be the supporting cells of stem cells. As shown in Fig. 7(E), the cristae between the limbus palisades (indicated by the arrow) is a highly reflective linear structure with bright, small, and irregularly shaped basal epithelial cells inside. The basal cells at the edge of the palisades of Vogt (POV) are highly reflective, and the cell boundaries are difficult to distinguish. Morphometry indicates that the size of these cells is significantly smaller than that of corneal basal cells (with a diameter of approximately 9-12  $\mu\text{m}$ ). Perform a 3D reconstruction of the limbus structure, as shown in Fig. 7(F), where highly reflective cells are concentrated in the basal layer of the limbus and unevenly distributed in the limbus region. The dual-mode FFOCT images of the superficial epithelial cells of the limbus are similar to the wing cells in the cornea. In the static image, the epithelial cells have high reflective cell boundaries and intracellular low reflection (see Fig. 7(G)). The dynamic image displays homogeneous functional signals within the cells, showing little differences amongst the epithelial cells in the same layer (see Fig. 7(H)). Dual-mode FFOCT imaging was performed on the basal layer cells of the limbus (see Fig. 7(I), (J)), and the cells with different manifestations in the static images exhibited varied dynamic images. For instance, the cell's shape and boundary are indistinguishable in the black box of Fig. 7(I) (magnified in Fig. 7(K)), whereas the dynamic image reveals the cell as a granular high-frequency signal (see Fig. 7(N)); In the red box of Fig. 7(I) (magnified in Fig. 7(L)) the high reflective cells with clear boundaries show homogeneous high-frequency signals in the dynamic image (see Fig. 7(O)); In the yellow box of Fig. 7(I) (magnified in Fig. 7(M)), the low reflective cells with unclear boundaries show low dynamic signals with indistinct cell contours in the dynamic image (see Fig. 7(P)). In the limbal stroma layer, static images show blood vessels or

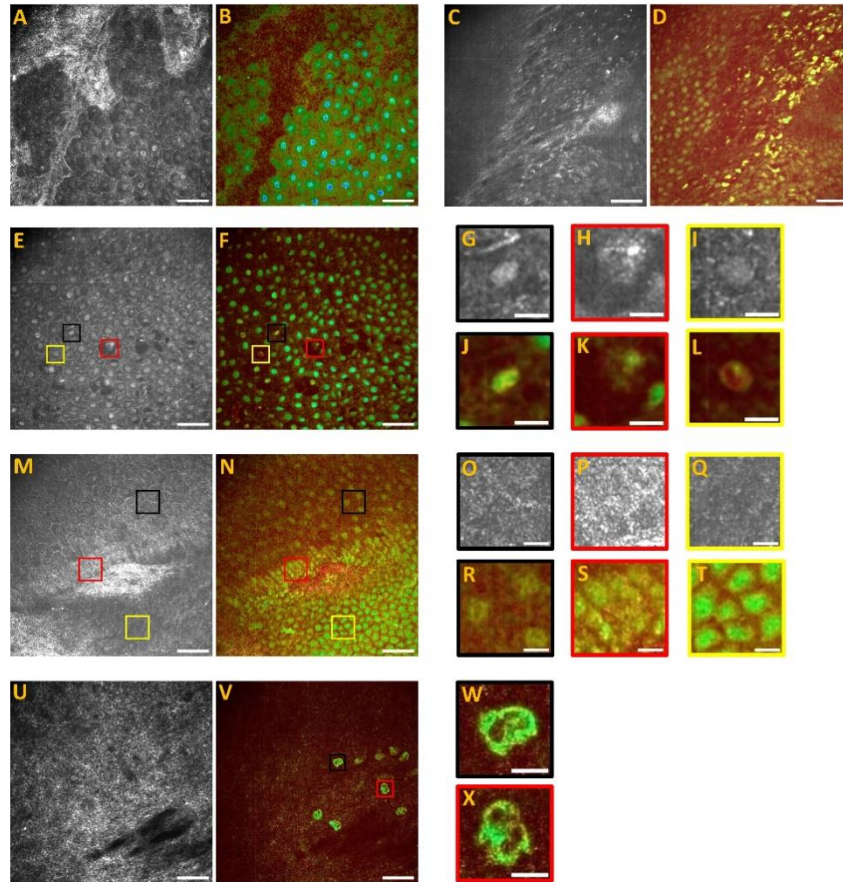


**Fig. 6.** Dual-mode FFOCT imaging of corneal leukoplakia epithelial cells. A, B: superficial epithelial cells. C, D: basal epithelial cells. E-T: different manifestations of epithelial cells in corneal leukoplakia samples due to different inflammatory responses. G-L: zoomed images of the ROIs marked in E and F. O-T: zoomed images of the ROIs marked in M and N. U: static image of scar fibrous tissue. V: dynamic image of inflammatory cells. W, X: zoomed images of the ROIs marked in V. (Scale-bar: A-F, M, N, U, V 50  $\mu\text{m}$ ; G-L, O-T, W, X 10  $\mu\text{m}$ )

lymphatic vessels (see Fig. 7(Q)), while dynamic images cannot display the static wall structure but instead highlight the cells located within the vessels (see Fig. 7(R)).

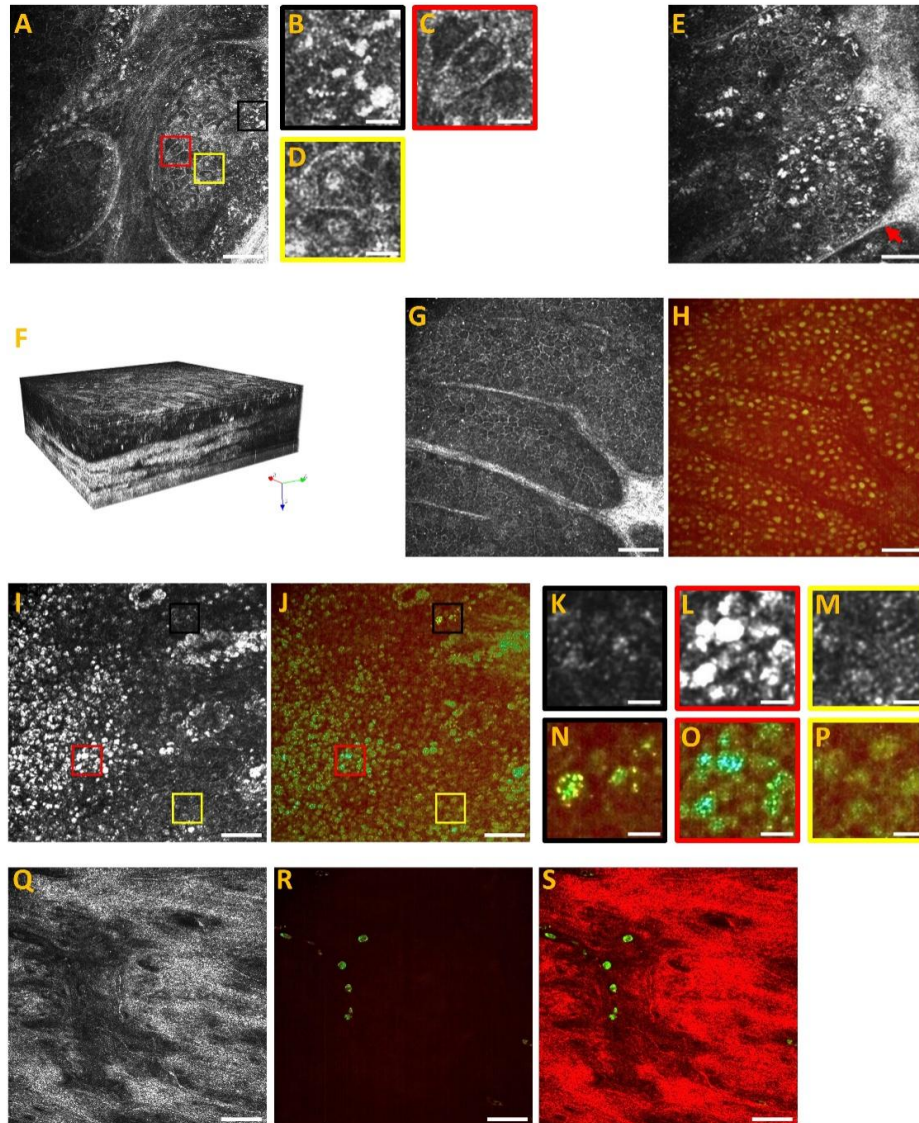


**Fig. 7.** Dual-mode FFOCT imaging of limbus. A: limbal crypt structure. B-D: epithelial cells with different manifestations in the limbal crypt. E: POV structure. The arrow points to cristae. F: 3D stack of *en face* static images of limbus. G, H: superficial epithelial cells in limbus. I-P: different manifestations of limbal basal cells. K-P: zoomed images of the ROIs marked in I and J. Q: static image of blood vessels or lymphatic vessels in limbal stroma. R: dynamic image of intraluminal cells. S: superimposed image of dual-mode images. (Scale-bar: A, E, G-J, Q-S 50  $\mu\text{m}$ ; B-D, K-P 10  $\mu\text{m}$ )

## 4. Discussion

In this study, dual-mode FF-OCT was used to image the donor cornea, pathological cornea, and limbus for the first time, which proved its complementary potential and dynamic contrast of high-resolution structural imaging and functional imaging of corneal tissue.

### 4.1. *Dual-mode FFOCT provides label-free images for donor cornea quality evaluation*

The meticulous assessment of donor corneal tissue quality constitutes a pivotal stage in ensuring the safety and efficacy of corneal transplantation procedures while concurrently mitigating postoperative transplant failure rates. This evaluation necessitates stringent adherence to aseptic protocols. Given the cornea's transparent optical nature and intricate structure, non-contact optical imaging technology emerges as a crucial modality for donor cornea quality assessment. Historically, the evaluation of corneal tissue quality in eye bank donors relied predominantly on slit-lamp microscopy and specular microscope, which rely on the experience of doctors for evaluation [44,45]. However, there are limitations in accurately imaging and evaluating the structure and morphology of cornea. Moreover, in clinical practice, the donor cornea's medical history may be incomplete, potentially lacking vital details such as a history of refractive surgery or keratoconus [46]. In our study, we demonstrated that dual-mode FFOCT imaging technology offers an enhanced and comprehensive approach to addressing these challenges in donor corneal quality evaluation, providing more precise insights into structural nuances and improving the overall efficacy of the assessment process.

Previous studies have demonstrated the correlation between FF-OCT images and conventional histological images, which can identify the different structures in normal cornea [47–49]. In this study, we first clearly demonstrated the ability of FFOCT structural imaging to identify different corneal structures in normal and diseased corneas. Clear imaging of the Bowman layer can detect features such as rupture, irregularity, scar formation, deposition, thinning, or loss, which are contraindications for penetrating or anterior lamellar keratoplasty but are currently difficult to detect in eye banks due to the lack of detection methods. FFOCT can evaluate the lamellar stroma in detail from the aspects of structure, quantity, thickness, reflectivity, and keratocyte density, which provides a new method for evaluating the condition and possible optical properties of donor corneal stroma. This is of great significance for the selection of donor tissue for penetrating keratoplasty or anterior lamellar keratoplasty. It is worth noting that corneal nerves are easily observed on the xy plane. Although corneal nerves have not been shown to directly affect the survival of corneal grafts, the lack of nerves affects the integrity of the corneal epithelium and the reinnervation of the grafts, which is essential for the survival of the grafts [50]. Therefore, FFOCT imaging has opened up a new dimension for evaluating the quality of donor corneas by understanding the state of preserved nerves.

On the other hand, by processing the spatial-temporal information of FFOCT dynamic interference signals, high-resolution cellular dynamic images based on endogenous metabolic activities of cells can also be obtained [33], providing non-invasive endogenous imaging information for the evaluation of cellular functional status [34,36]. The potential biological processes that cause the dynamic contrast are related to cell metabolism and may include the movement of organelles such as mitochondria, Golgi bodies, lysosomes, vesicles, and pigments [33,36]. In our study, we demonstrated that D-FFOCT can perform full-layer imaging of individual cells in the entire corneal tissue, particularly highlighting the endogenous signals of epithelial cells, which compensates for the possibility that sub-surface epithelial signals may be masked by strong surface reflections in static images. Previous experiment [35] has shown that D-FFOCT can be used to distinguish different states of cells (such as normal, dying, or dead cells). We found that the epithelial cells of corneal grafts may exist in various states, including division, death, and homeostasis, which are typically assessed via intracellular functional signals and cell morphology. There is a relationship between the functional signals of corneal epithelial

cells and the quality of corneal grafts. In edematous corneal graft samples, cellular function loss may occur in the superficial and even deeper layers of the cornea. In transplantation scenarios, the epithelial cells of the corneal grafts must remain active to ensure proper corneal function. If these cells become damaged or inactive, it could lead to postoperative complications, including chronic epithelial defects or corneal epithelial tears [51]. Nevertheless, scant scholarly inquiry has been dedicated to the assessment of corneal epithelium condition in corneal grafts, primarily ascribed to the prevailing constraints inherent in non-invasive diagnostic tools.

Dual-mode FFOCT stands as a potent non-invasive modality, facilitating anatomical examinations and quantitative analyses of the cornea over a broad field of view. Additionally, its capability for cell-level functional imaging provides detailed insights. Integrating dual-mode FFOCT diagnostics into the standard assessment procedures of eye bank donor corneas represents a substantial advancement. This augmentation aims to systematically appraise the quality of stored specimens, allowing for a meticulous selection process that identifies the most suitable corneas for transplantation. This strategic incorporation of dual-mode FFOCT has the potential to enhance postoperative outcomes significantly, mitigating the risk of complications associated with corneal transplantation.

#### *4.2. Dual-mode FFOCT highlights cellular changes for corneal pathological diagnosis*

Corneal pathological diagnosis helps to determine the type of disease and extent of lesions, thereby clarifying the progression of the disease and assisting in selecting appropriate treatment options. Apoptosis is a prevalent physiological phenomenon in corneal tissue, serving as a vital mechanism for preserving tissue homeostasis [6]. To maintain the health of the cornea, corneal cells undergo apoptosis at periodic intervals within normal circumstances [7]. In pathological states, corneal cells frequently undergo atypical cell death, which can encompass various cell death modalities such as apoptosis, necrosis, and other types [5,52]. For instance, some studies indicated that there may be a surge in apoptosis cells among keratoconus [53]. In our study, we observed the existence of corneal epithelial cells that were deformed and morphologically atrophic on keratoconus samples, resulting in a loss of nuclear signals and cell boundary signals that were blurry and indiscernible in dynamic images. Swelling of some keratoconus epithelial cells was observed, displaying an inhomogeneous cytoplasm with granular high-frequency signals and nuclei characterized by blurred boundaries with functional signals. This phenomenon is comparable to the formation of vesicles during the process of cell apoptosis described in pathology [54], demonstrating that dual-mode FFOCT is capable of detecting dynamic intracellular activity and cytoskeletal changes in samples of lesions. Inflammatory lesions within the corneal tissue, including infiltration of Langerhans cells, neovascularization, or nascent lymphatic vessels, are identifiable through dual-mode FFOCT imaging. we found that static images obstruct the visualization of inflammatory cells due to highly refractive scars, blood vessel walls, or lymphatic tissue. In contrast, dynamic images can highlight inflammatory cells in low-contrast and weak-signal imaging, with the nuclei of inflammatory cells being visible. This provides an approximation of inflammatory cell types in pathological histology, based on the shape of their nuclei. This means that dual-mode FFOCT can not only detect the progression of inflammation but also provide auxiliary diagnostic evidence in determining the type of inflammation, thereby helping doctors to select the appropriate treatment plans. Dual-mode FFOCT, as a high-resolution microscopy technique, can directly visualize the structure and metabolism of living corneal cells. It is valuable in evaluating and diagnosing corneal lesions, infections, and inflammation. Additionally, multi-modality imaging can be used to increase contrast and provide supplemental information beyond structure. These findings require further validation and subsequent investigation of the potential impact on D-FFOCT signals during the development of corneal lesions. Nevertheless, they present an inventive and practical alternative



for utilizing this method to diagnose pathology without the need for any preparation or staining steps.

#### 4.3. Dual-mode FFOCT is promising for limbus evaluation

Autologous or allogeneic limbus grafts, along with in vitro cultivated autologous LSCs transplantation, prove to be effective treatments for LSCD [55]. Identification and characterization of LSCs in the graft material, along with functional quality testing before the transplantation procedure, are essential to ensure successful postoperative reconstruction of the corneal surface [56]. Previous studies have utilized impression cytology corneal scraping and culturing, flow cytometry, immunohistochemistry, polymerase chain reaction (PCR), and electron microscopy to analyze the properties and functions of LSCs [57–61]. However, these methods are not non-invasive and require additional cell staining or modifications. Furthermore, the assay results are directly dependent on the quality of the sampling collected. The examination of limbus structure and function, especially the role of LSCs, has always been a pioneering and noteworthy subject in the field of ophthalmology. With the development and innovation of imaging technology, non-invasive, objective, high-precision, and reproducible imaging methods have emerged as crucial auxiliary tools in ophthalmic diagnosis and treatment. AS-OCT provides cross-sectional images of the anterior segment, including the limbus [11], but cannot achieve structural imaging at the cellular level. IVCN can visualize the microstructure of the corneal limbus at the cellular level [62], but its imaging is limited by the field of view and lacks specificity to provide direct information about cells. In our research, it was demonstrated that dual-mode FFOCT technology permits the capturing of cellular-level structural and dynamic functional imaging of limbus tissues, facilitating high-resolution 3D images that allow for observation of the distribution of limbal cells. Limbal palisades of Vogt structures, wherein LSCs are predominantly distributed, are observable distinctly in *en face* maps at different depths, indicating differences in image reflectivity and functional signals between cells, which may represent multiple types of cells in the limbal niche. A significant quantity of bright, small, and irregular basal epithelial cells with active intracellular functional signals are visible within the basal layer of the limbus. Previous research has indicated that distinguishing LSCs from mature corneal epithelium may be achieved through morphological evaluation of the cells. In vitro-cultured LSCs are typically small ( $\leq 12 \mu\text{m}$  in diameter) and rounded, exhibiting a distinctive “cobblestone” shape and a relatively large ratio of nucleoplasm [63,64]. In our experiment, it is currently unclear whether the endogenous high-frequency signals of these cells are indicative of low differentiation and high proliferative capacity of the epithelial cells. This uncertainty is due to the homeostatic environment of the samples used in the experiment and the short duration of the assay. In subsequent studies, dual-mode FFOCT can be employed on organoids attained from LSCs cultured in vitro to monitor the activity and dynamic processes of LSCs, such as migration and differentiation. Overall, dual-mode FFOCT provides comprehensive information about the microstructure and characteristics of the limbus, which is crucial for studying the role of LSCs in corneal maintenance and repair. Through dual-mode FFOCT, scientists can gain a superior comprehension of the biological characteristics and functions of LSCs.

#### 4.4. Limitations and future work

There are certain limitations in our current study and technique. Due to limited number and types of human cornea samples were obtained, no comparative statistical analysis was conducted in current study to differentiate healthy and pathological corneas quantitatively. Future work will be continued by including more types of cornea samples, expanding the sample size and conducting comprehensive statistical analysis to establish normative baselines as well as qualitative and quantitative biomarkers donor and pathological corneas with dual-mode FFOCT. In this study, only ex vivo corneas were imaged with dual-mode FFOCT, primarily due to the susceptibility of

dynamic FFOCT to eye motions. Though the system imaging speed has been greatly improved and motion artefacts removal algorithms have been applied, transitioning dynamic FFOCT from ex vivo experiments to in vivo applications still face technical challenges. Addressing these challenges is crucial for its potential application as a diagnostic tool for in vivo assessment of corneal pathology.

## 5. Conclusion

Dual-mode FFOCT demonstrates promising results in imaging the cornea and limbus. This advanced technology provides clear, high-resolution *en face* images of cellular structures in unfixed and unlabeled corneas, including pathological samples. Notably, it captures dynamic contrast from endogenous cell motility, offering detailed insights into structural and functional changes at the cellular level. The technique's ability to highlight epithelial cell differences in normal and pathological corneas without contrast agent labeling makes dual-mode FFOCT a potentially valuable tool for cellular-level exploration in ophthalmology.

**Funding.** National Natural Science Foundation of China (82230033, 82271133); Guangdong Provincial Department of Science and Technology (2021TQ06Y137, 2021TX06Y127); Basic and Applied Basic Research Foundation of Guangdong Province (2022A1515011486); Fundamental Research Funds of the State Key Laboratory of Ophthalmology.

**Acknowledgments.** The authors thank Dr. Bowen Wang and Dr. Lulu Peng for assistance in sample collection, Jiaxiong Li and Ke Ma for guidance in image processing, and Dr. Yuqing Deng for helpful advice in image interpretation.

**Disclosures.** The authors declare that the research was conducted in the absence of any commercial or financial relationships that could be construed as a potential conflict of interest.

**Data availability.** Data underlying the results presented in this paper are not publicly available at this time but could be obtained from the authors upon reasonable request.

## References

1. D. W. DelMonte and T. Kim, "Anatomy and physiology of the cornea," *J. Cataract Refractive Surg.* **37**(3), 588–598 (2011).
2. M. S. Sridhar, "Anatomy of cornea and ocular surface," *Indian J. Ophthalmol.* **66**(2), 190–194 (2018).
3. A. O. Eghrari, S. A. Riazuddin, and J. D. Gottsch, "Overview of the cornea: structure, function, and development," *Progress in Molecular Biology and Translational Science* **134**, 7–23 (2015).
4. S. Kinoshita, W. Adachi, C. Sotozono, *et al.*, "Characteristics of the human ocular surface epithelium," *Prog. Retinal Eye Res.* **20**(5), 639–673 (2001).
5. C.-Y. Liu and W. W.-Y. Kao, "Corneal epithelial wound healing," *Progress in Molecular Biology and Translational Science* **134**, 61–71 (2015).
6. S. E. Wilson, "Role of apoptosis in wound healing in the cornea," *Cornea* **19**(Supplement 1), S7–S12 (2000).
7. S. E. Wilson, "Corneal wound healing," *Exp. Eye Res.* **197**, 108089 (2020).
8. C. Bonnet, S. González, J. S. Roberts, *et al.*, "Human limbal epithelial stem cell regulation, bioengineering and function," *Prog. Retinal Eye Res.* **85**, 100956 (2021).
9. S. C. Tseng, "Concept and application of limbal stem cells," *Eye* **3**(2), 141–157 (1989).
10. G. Yazdanpanah, Z. Haq, K. Kang, *et al.*, "Strategies for reconstructing the limbal stem cell niche," *The Ocular Surface* **17**(2), 230–240 (2019).
11. Y. Feng and T. L. Simpson, "Comparison of human central cornea and limbus in vivo using optical coherence tomography," *Optometry and Vision Science* **82**(5), 416–419 (2005).
12. Y. F. G. Marin, D. Alonso-Caneiro, S. J. Vincent, *et al.*, "Anterior segment optical coherence tomography (AS-OCT) image analysis methods and applications: a systematic review," *Comput. Biol. Med.* **146**, 105471 (2022).
13. E. Villani, C. Baudouin, N. Efron, *et al.*, "In vivo confocal microscopy of the ocular surface: from bench to bedside," *Curr. Eye Res.* **39**(3), 213–231 (2014).
14. P. Tankam, Z. He, Y.-J. Chu, *et al.*, "Assessing microstructures of the cornea with Gabor-domain optical coherence microscopy: pathway for corneal physiology and diseases," *Opt. Lett.* **40**(6), 1113–1116 (2015).
15. K. Bizheva, B. Tan, B. MacLellan, *et al.*, "Sub-micrometer axial resolution OCT for in-vivo imaging of the cellular structure of healthy and keratoconic human corneas," *Biomed. Opt. Express* **8**(2), 800–812 (2017).
16. X. Yao, K. Devarajan, R. M. Werkmeister, *et al.*, "In vivo corneal endothelium imaging using ultrahigh resolution OCT," *Biomed. Opt. Express* **10**(11), 5675–5686 (2019).
17. B. Tan, Z. Hosseinaee, L. Han, *et al.*, "250 kHz, 1.5  $\mu$ m resolution SD-OCT for in-vivo cellular imaging of the human cornea," *Biomed. Opt. Express* **9**(12), 6569–6583 (2018).
18. L. Han, B. Tan, Z. Hosseinaee, *et al.*, "Line-scanning SD-OCT for in-vivo, non-contact, volumetric, cellular resolution imaging of the human cornea and limbus," *Biomed. Opt. Express* **13**(7), 4007–4020 (2022).

19. K. Neuhaus, S. Khan, O. Thaware, *et al.*, “Real-time line-field optical coherence tomography for cellular resolution imaging of biological tissue,” *Biomed. Opt. Express* **15**(2), 1059–1073 (2024).
20. K. Chen, W. Song, L. Han, *et al.*, “Powell lens-based line-field spectral domain optical coherence tomography system for cellular resolution imaging of biological tissue,” *Biomed. Opt. Express* **14**(5), 2003–2014 (2023).
21. E. Beurepaire, A. C. Boccara, M. Lebec, *et al.*, “Full-field optical coherence microscopy,” *Opt. Lett.* **23**(4), 244–246 (1998).
22. A. Dubois, K. Grieve, G. Moneron, *et al.*, “Ultra-high-resolution full-field optical coherence tomography,” *Appl. Opt.* **43**(14), 2874–2883 (2004).
23. A. Dubois, L. Vabre, A.-C. Boccara, *et al.*, “High-resolution full-field optical coherence tomography with a Linnik microscope,” *Appl. Opt.* **41**(4), 805–812 (2002).
24. P. Xiao, M. Fink, and A. C. Boccara, “Full-field spatially incoherent illumination interferometry: a spatial resolution almost insensitive to aberrations,” *Opt. Lett.* **41**(17), 3920–3923 (2016).
25. V. Mazlin, P. Xiao, E. Dalimier, *et al.*, “In vivo high resolution human corneal imaging using full-field optical coherence tomography,” *Biomed. Opt. Express* **9**(2), 557–568 (2018).
26. J. Zhang, V. Mazlin, K. Fei, *et al.*, “Time-domain full-field optical coherence tomography (TD-FF-OCT) in ophthalmic imaging,” *Ther. Adv. Chronic Dis.* **14**, 204062232311701 (2023).
27. V. Mazlin, P. Xiao, J. Scholler, *et al.*, “Real-time non-contact cellular imaging and angiography of human cornea and limbus with common-path full-field/SD OCT,” *Nat. Commun.* **11**(1), 1868 (2020).
28. P. Xiao, V. Mazlin, K. Grieve, *et al.*, “In vivo high-resolution human retinal imaging with wavefront-correctionless full-field OCT,” *Optica* **5**(4), 409–412 (2018).
29. E. Aukorius, D. Borycki, P. Stremplewski, *et al.*, “In vivo imaging of the human cornea with high-speed and high-resolution Fourier-domain full-field optical coherence tomography,” *Biomed. Opt. Express* **11**(5), 2849–2865 (2020).
30. I. Abd El-Sadek, L. T.-W. Shen, T. Mori, *et al.*, “Label-free drug response evaluation of human derived tumor spheroids using three-dimensional dynamic optical coherence tomography,” *Sci. Rep.* **13**(1), 15377 (2023).
31. T. Kohlfaerber, M. Pieper, M. Münter, *et al.*, “Dynamic microscopic optical coherence tomography to visualize the morphological and functional micro-anatomy of the airways,” *Biomed. Opt. Express* **13**(6), 3211–3223 (2022).
32. G. Musial, T. Kohlfaerber, M. Ahrens, *et al.*, “Dynamic contrast microscopic optical coherence tomography as a novel method for assessing corneal epithelium during exposure to benzalkonium chloride,” *Ther. Adv. Chronic Dis.* **11**(5), 28 (2022).
33. C. Apelian, F. Harms, O. Thouvenin, *et al.*, “Dynamic full field optical coherence tomography: subcellular metabolic contrast revealed in tissues by interferometric signals temporal analysis,” *Biomed. Opt. Express* **7**(4), 1511–1524 (2016).
34. K. Groux, A. Verschuere, C. Nanteau, *et al.*, “Dynamic full-field optical coherence tomography allows live imaging of retinal pigment epithelium stress model,” *Commun. Biol.* **5**(1), 575 (2022).
35. S. Park, T. Nguyen, E. Benoit, *et al.*, “Quantitative evaluation of the dynamic activity of HeLa cells in different viability states using dynamic full-field optical coherence microscopy,” *Biomed. Opt. Express* **12**(10), 6431–6441 (2021).
36. J. Scholler, K. Groux, O. Goureau, *et al.*, “Dynamic full-field optical coherence tomography: 3D live-imaging of retinal organoids,” *Light: Sci. Appl.* **9**(1), 140 (2020).
37. J. Scholler, V. Mazlin, O. Thouvenin, *et al.*, “Probing dynamic processes in the eye at multiple spatial and temporal scales with multimodal full field OCT,” *Biomed. Opt. Express* **10**(2), 731–746 (2019).
38. S. Labiau, G. David, S. Gigan, *et al.*, “Defocus test and defocus correction in full-field optical coherence tomography,” *Opt. Lett.* **34**(10), 1576–1578 (2009).
39. J. Scholler, “Motion artifact removal and signal enhancement to achieve in vivo dynamic full field OCT,” *Opt. Express* **27**(14), 19562–19572 (2019).
40. J. Schindelin, I. Arganda-Carreras, E. Frise, *et al.*, “Fiji: an open-source platform for biological-image analysis,” *Nat. Methods* **9**(7), 676–682 (2012).
41. K. A. Sterenczak, K. Winter, K. Sperlich, *et al.*, “Morphological characterization of the human corneal epithelium by in vivo confocal laser scanning microscopy,” *Quantitative imaging in medicine and surgery* **11**(5), 1737–1750 (2021).
42. E. B. Ozgurhan, N. Kara, A. Yildirim, *et al.*, “Evaluation of corneal microstructure in keratoconus: a confocal microscopy study,” *Am. J. Ophthalmol.* **156**(5), 885–893.e2 (2013).
43. D. V. Patel and C. N. McGhee, “Mapping the corneal sub-basal nerve plexus in keratoconus by in vivo laser scanning confocal microscopy,” *Invest. Ophthalmol. Vis. Sci.* **47**(4), 1348–1351 (2006).
44. S. Chaurasia and M. Vanathi, “Specular microscopy in clinical practice,” *Indian J. Ophthalmol.* **69**(3), 517–524 (2021).
45. M. Patil, A. Lune, R. Paranjape, *et al.*, “Qualitative and quantitative evaluation of donor corneal tissue by slit lamp and specular microscopy,” *Cureus* **14**(5), e24700 (2022).
46. J. C. Mora, “Objective screening methods for prior refractive surgery in donor tissue,” *Annals d’oftalmologia: òrgan de les Societats d’Oftalmologia de Catalunya, Valencia i Balears* **21**(2), 181–188 (2002).
47. M. Akiba, N. Maeda, K. Yumikake, *et al.*, “Ultra-high-resolution imaging of human donor cornea using full-field optical coherence tomography,” *J. Biomed. Opt.* **12**(4), 041202 (2007).

48. W. Ghouali, K. Grieve, S. Bellefqih, *et al.*, “Full-field optical coherence tomography of human donor and pathological corneas,” *Curr. Eye Res.* **40**(5), 526–534 (2015).
49. M. Borderie, K. Grieve, K. Irsch, *et al.*, “New parameters in assessment of human donor corneal stroma,” *Acta Ophthalmol.* **95**, e297–e306 (2017).
50. V. K. Dhillon, M. S. Elalfy, M. Messina, *et al.*, “Survival of corneal nerve/sheath structures in organ-cultured donor corneas,” *Acta Ophthalmol.* **96**, e334–e340 (2018).
51. S. Feizi, M. A. Javadi, H. Ghasemi, *et al.*, “Effect of donor graft quality on clinical outcomes after penetrating keratoplasty for keratoconus,” *J. Ophthalmic Vision Res.* **10**(4), 364 (2015).
52. R. S. Hotchkiss, A. Strasser, J. E. McDunn, *et al.*, “Cell death,” *N. Engl. J. Med.* **361**(16), 1570–1583 (2009).
53. R. M. Kaldawy, J. Wagner, S. Ching, *et al.*, “Evidence of apoptotic cell death in keratoconus,” *Cornea* **21**(2), 206–209 (2002).
54. K.-Y. Han, J. A. Tran, J.-H. Chang, *et al.*, “Potential role of corneal epithelial cell-derived exosomes in corneal wound healing and neovascularization,” *Sci. Rep.* **7**(1), 40548 (2017).
55. S. X. Deng, F. Kruse, J. A. Gomes, *et al.*, “Global consensus on the management of limbal stem cell deficiency,” *Cornea* **39**(10), 1291–1302 (2020).
56. M. de Almeida Fuzeta, A. D. de Matos Branco, A. Fernandes-Platzgummer, *et al.*, “Addressing the manufacturing challenges of cell-based therapies,” *Adv Biochem Eng Biotechnol* **171**, 225–278 (2020).
57. A. L. Araújo, J. R. Ricardo, V. N. Sakai, *et al.*, “Impression cytology and in vivo confocal microscopy in corneas with total limbal stem cell deficiency,” *Arq. Bras. Oftalmol.* **76**(5), 305–308 (2013).
58. A. Kate and S. Basu, “A review of the diagnosis and treatment of limbal stem cell deficiency,” *Front. Med.* **9**, 836009 (2022).
59. M. López-Paniagua, T. Nieto-Miguel, A. de la Mata, *et al.*, “Consecutive expansion of limbal epithelial stem cells from a single limbal biopsy,” *Curr. Eye Res.* **38**(5), 537–549 (2013).
60. N. Genicio, J. Gallo Paramo, and A. J. Shortt, “Quantum dot labeling and tracking of cultured limbal epithelial cell transplants in vitro,” *Invest. Ophthalmol. Vis. Sci.* **56**(5), 3051–3059 (2015).
61. A. K. Kureshi, R. A. Drake, and J. T. Daniels, “Challenges in the development of a reference standard and potency assay for the clinical production of RAFT tissue equivalents for the cornea,” *Regen Med* **9**(2), 167–177 (2014).
62. M. Tavakoli, P. Hossain, and R. A. Malik, “Clinical applications of corneal confocal microscopy,” *Clin Ophthalmol* **9**(2), 167–445 (2014).
63. G. Pellegrini, O. Golisano, P. Paterna, *et al.*, “Location and clonal analysis of stem cells and their differentiated progeny in the human ocular surface,” *J Cell Biol* **145**(4), 769–782 (1999).
64. A. C. Romano, E. M. Espana, S. H. Yoo, *et al.*, “Different cell sizes in human limbal and central corneal basal epithelia measured by confocal microscopy and flow cytometry,” *Invest. Ophthalmol. Vis. Sci.* **44**(12), 5125–5129 (2003).